Journal of Biomedical Materials Research Part A

WILEY

Society For Biomaterials

RESEARCH ARTICLE OPEN ACCESS

Exploring the Reactions Induced by Bioactive Glass Air Abrasion of Titanium and Their Effects on Osteoblast Cellular Responses

Faleh Abushahba[1,2] | Adrian Stiller[3] | Sherif A. Mohamad[4] | Nagat Areid[2] | Leena Hupa[3] | Terhi J. Heino[4] | Pekka K. Vallittu[1,5] | Timo O. Närhi[2,5]

[1]Department of Biomaterials Science and Turku Clinical Biomaterials Center—TCBC, Institute of Dentistry, University of Turku, Turku, Finland | [2]Department of Prosthetic Dentistry and Stomatognathic Physiology, Institute of Dentistry, University of Turku, Turku, Finland | [3]Johan Gadolin Process Chemistry Centre, Åbo Akademi University, Turku, Finland | [4]Institute of Biomedicine, Faculty of Medicine, University of Turku, Turku, Finland | [5]The Wellbeing Service County Southwest Finland, Turku, Finland

Correspondence: Faleh Abushahba (fafabu@utu.fi)

Received: 20 February 2025 | **Revised:** 16 May 2025 | **Accepted:** 3 June 2025

Funding: This work was supported by Business Finland Co-innovation.

Keywords: bioactive glass | calcium phosphate | implant surface | mineralization | peri-implantitis | zinc

ABSTRACT

This study investigated the chemical events that occur when titanium (Ti) surfaces are treated with air particle abrasion (APA) using zinc-containing bioactive glass (ZnBG), followed by immersion in simulated body fluid (SBF) for up to 96 h. The impact of these changes on osteoblast cell viability, adhesion, and differentiation was evaluated. Sandblasted and acid-etched (SA) Ti disks were subjected to APA with ZnBG particles and then immersed in SBF from 8 to 96 h. Ion dissolution and characterization of ZnBG powder and Ti disks were conducted. Analyses of osteoblast viability, adhesion, and alkaline phosphatase (ALP) activity were performed on MC3T3-E1 cells cultured on control disks (SA-Ti), as well as on ZnBG abraded disks (APA-Ti) and disks immersed for 96 h in SBF (CaP-Ti). After SBF immersion, the ZnBG particle surfaces showed a rise in Si atomic (at.)% within the first 8 h, while Ca remained stable, and the P doubled over 96 h. The ZnBG covering the disks dissolved during the first 8 h, and then the Ca, P, and Si at.% increased as the immersion time extended. The glass particles exhibited amorphous calcium–phosphate (Ca–P) layer formation after 96 h. A significantly ($p = 0.004$) higher cell viability level was observed on day 7 on APA-Ti compared to SA-Ti disks, while no differences in osteoblast differentiation were observed across the different surfaces. Fluorescence images demonstrated that on day 3, cells adhered to valleys and peaks of CaP-Ti threads but only to valleys on SA-Ti and APA-Ti disks. By day 7, cells were also observed on APA-Ti peaks but not on SA-Ti. In summary, APA enhanced osteoblast proliferation, and a biocompatible Ca–P layer, which formed upon mineralization, supported osteoblast viability, adhesion, and spreading.

1 | Introduction

Peri-implantitis (PI) is a common inflammatory condition triggered by the formation of a complex biofilm on implant surfaces. This film induces an inflammatory reaction, resulting in progressive, irreversible loss of implant-supporting tissues [1–3]. Accordingly, most treatment strategies focus on implant biofilm surface decontamination. However, implants' micro- and

macro-surface configurations are known to facilitate biofilm retention and impede adequate debridement, leading to inadequate treatment outcomes [4, 5]. A universally accepted golden standard method for implant surface biofilm decontamination has not yet been established.

Air particle abrasion (APA) utilizing bioactive glasses (BG), including 45S5 BG and zinc-containing BG (ZnBG), has shown in vitro effectiveness in decontaminating sandblasted and acid-etched (SA) titanium (Ti) surfaces coated with bacterial biofilms commonly associated with PI [6–8]. Furthermore, APA can lead to the firm attachment of BG particles to the Ti surface [9] and provide a prolonged antibacterial effect against bacterial colonization and biofilm formation on the implant surface [6, 7, 9].

The antibacterial activity of BG is primarily attributed to their high chemical reactivity in physiological environments. Upon exposure to aqueous solutions, such as simulated body fluid (SBF), BG undergo a series of surface reactions. In the early stages, network-modifying ions such as sodium (Na^+) and calcium (Ca^{2+}) are released via ion exchange with protons (H^+) from the surrounding medium [10, 11]. This process increases the local hydroxide ions (OH^-) concentration, leading to elevated pH and osmolarity. The resulting alkaline, hypertonic microenvironment is unfavorable to microbial viability and contributes to the antibacterial properties of BG [12–14]. In addition, the selective depletion of Na^+ and Ca^{2+} ions produces a silica-enriched surface, which undergoes hydrolysis and condensation to form a hydrated, porous silica-rich layer over time. This evolving interfacial layer serves as a scaffold for calcium–phosphate (Ca–P) nucleation and growth [15, 16]. As mineralization progresses, a bi-layered surface forms, consisting of an inner silica-rich region and an outer hydroxyapatite (HA) phase. This structural transformation not only affects the dissolution behavior of the material but also modulates surface chemistry and topography, with potential consequences for cell–material interactions and biological responses [17].

We have previously demonstrated that air abrasion of grit-blasted and acid-etched Ti surfaces with ZnBG enhanced osteoblast proliferation and viability compared to unabraded controls [18], indicating improved early-stage surface biocompatibility. However, this effect appeared transient: after 14 days of immersion in SBF, osteoblast behavior on ZnBG-abraded surfaces was comparable to that observed on unabraded controls [19]. These findings suggest that time-dependent physicochemical changes at the ZnBG-treated surface may influence its ability to support cellular function.

To investigate these time-dependent changes, this study evaluated surface composition and morphology alterations over a 96-h immersion period, alongside monitoring ion concentrations in the surrounding medium. In parallel, osteoblast viability, adhesion, and differentiation were assessed on the evolving surfaces. By integrating chemical, physical, and biological analyses, this study aims to provide mechanistic insight into how dynamic surface transformations influence the biological performance of BG-functionalized implant materials.

2 | Materials and Methods

2.1 | Titanium Disk Preparation

A Grade II square Ti plate of 200 x 200 mm in size and 1 mm in thickness was used to prepare the Ti disks. The plate was thread-milled and then cut into smaller Ti disks (7 × 7 mm). For SA-Ti surface preparation of the disks, the threaded side of the disks was first sandblasted with Al_2O_3 particles (250–500 μm), followed by acid-etching in a mixture of HCl (60%) and H_2SO_4 (70%) for 60 min at 60°C in a hot air oven.

2.2 | Glass Sample Preparation

The experimental ZnBG, with a nominal oxide composition of 44.1 SiO_2–24.3 Na_2O–24.9 CaO–2.6 P_2O_5–4.0 ZnO_4 (mol.%). To prepare a 300 g glass block, a raw material batch was mixed from burned Belgian glass-quality quartz sand (0.32 mm, Varnia Oy) and the analytical-grade chemicals sodium carbonate (Na_2CO_3; Fluka), calcium carbonate ($CaCO_3$; Fluka), calcium hydrogen phosphate dihydrate ($CaHPO_4 \cdot _2H_2O$; Thermo Scientific), and zinc oxide (ZnO; Sigma-Aldrich). The glass was melted in air in an uncovered platinum crucible at 1360°C for 3 h. After casting, the obtained glass block was annealed at 520°C for 1 h and then cooled to room temperature in the oven. The glass block was crushed and remelted to improve compositional homogeneity. A laboratory ring-and-puck mill was used to grind glass particles. The particles were then sieved to obtain a size fraction of 20–125 μm and cleaned three times in an ultrasonic bath with fresh acetone to remove any fine glass powder residues. After cleaning, the particles were dried overnight at 60°C. Prior to use, the glass particles were stored in a desiccator.

2.2.1 | Particle Size Analysis

The particle size distributions (PSDs) of the sieved ZnBG particles were determined by laser diffraction analysis (LDA) using a laser diffraction system (Mastersizer 3000, Malvern Instruments Ltd., Worcestershire, UK) paired with a wet dispersion unit (Malvern Hydro EV). Measurements involved sequential use of a red-light source (max. 4 mW, He-Ne, 632.8 nm) and a blue light source (nominal 10 mW LED, 470 nm). The system was operated with MasterSizer 3000 software (v3.63). The Mie theory was selected to analyze the nonspherical particles, and results were reported as volume equivalent sphere diameters. Analytical-grade ethanol (99.8%) was used as the dispersant. The refractive index of ZnBG was set to 1.56, and that of the dispersant, ethanol, was set to 1.36. The background was measured in ethanol before adding the glass particles to achieve an obscuration level of ~19.0%. A high stirring speed ensured turbulent flow and random particle orientation. Three representative samples were each measured five times, and the average particle size distribution was calculated from these replicates.

2.3 | Air Particle Abrasion of SA Ti Disks

The threaded side of the SA-Ti disks was subjected to ZnBG APA using an air-abrasive device (LM ProPower; LM, Parainen,

Finland) with the glass particle size specified above. For APA-Ti disk preparation, each SA-Ti disk was subjected to APA for a duration of 20 s, at an angle of 90°, from a distance of 3 mm. A pressure setting of 4 kPa was applied at the pressure outlet insertion point and the air-polishing device inlet.

2.4 | Immersion Experiments and Ion Concentration Measurements

The APA-Ti disks were immersed in SBF, which had been prepared according to the protocol by Kokubo and Takadama [20] (Table 1). The immersion experiments were performed in triplicate for 8, 24, 48, and 72 h and in five replicates for 96 h. For each experiment, 100 mg of loose ZnBG particles of the same size used for the APA were placed into a 50 mL conical centrifuge tube. A stainless-steel woven mesh was inserted above the conical section of the tube, and an APA-Ti disk was positioned so that the threads' side faced up on the mesh. The experiments began by adding 20 mL of SBF to each tube. The tubes were then placed in a shaking incubator set to 37°C and 120 RPM. After immersion, the solution was filtered into a clean 50 mL container, and the reacted particles and disks were rinsed with analytical-grade ethanol. The particles and the disks were dried overnight at 37°C and stored in a desiccator until further analysis.

Ion concentrations in solution were analyzed using inductively coupled plasma optical emission spectrometry (ICP-OES, Optima 5300 DV; Perkin Elmer, Waltham, USA). Solution samples collected in the immersion experiments were diluted with ultrapure water at ratios of 1:10 and 1:20 and acidified with 3% (v/v) concentrated nitric acid (65 wt.%; Suprapur, Merck). The average ion concentrations at different time points in the immersion experiments were determined from the measured concentrations of replicate samples at the different dilutions. The ICP-OES device was calibrated using ultrapure water and certified single-element (for Si, P, K) and multielement (for Na, Mg, Ca, Zn) standards (all: Spectrascan, Teknolab AS, Norway, except for K: Ultra Scientific, Agilent Technologies, USA). Calibration was performed using a dilution series of 0, 1, 5, and 20 ppm for all elements. The following emission lines and configurations were used for analysis: Ca ($\lambda = 315.887$ nm, axial; $\lambda = 315.887$ nm, radial); K ($\lambda = 766.490$ nm, radial); Mg ($\lambda = 285.213$ nm, radial); Na ($\lambda = 589.592$ nm, radial); P ($\lambda = 213.617$ nm, axial); Si ($\lambda = 251.611$ nm; axial); Zn ($\lambda = 213.857$ nm, radial). Each ICP-OES sample measurement consisted of five single scans.

TABLE 1 | Composition, order, and amounts of reagents used to prepare 1000 mL of simulated body fluid (SBF) according to Kokubo and Takadama [20].

Order	Reagent	Amount
1	NaCl	8.035 g
2	$NaHCO_3$	0.355 g
3	KCl	0.225 g
4	$K_2HPO_4.3H_2O$	0.231 g
5	$MgCl_2.6H_2O$	0.311 g
6	1.0 M-HCl	39 mL
7	$CaCl_2$	0.292 g
8	Na_2SO_4	0.072 g
9	Tris	6.118 g
10	1.0 M-HCl	0–5 mL

2.5 | Characterization of Glass Particles and Ti Disks

2.5.1 | Microscopic Analysis

The morphology and surface composition of glass particles and Ti disks were analyzed using scanning electron microscopy (SEM, Leo 1530, Oberkochen, Germany) combined with energy-dispersive X-ray analysis (EDX, UltraDry, Thermo Scientific, Madison, USA). The glass particles were dispersed on double-sided adhesive carbon conductive tape attached to an aluminum plate holder. The Ti disks were mounted face-up on an aluminum plate holder using carbon conductive tape and then sputtered with platinum. Analyses were conducted on particles both before and after the immersion experiments. The Ti disks examined included SA-Ti, APA-Ti, and those subjected to immersion experiments. Three disks from each group were studied in parallel.

2.5.2 | X-Ray Diffraction Analysis

X-ray diffraction (XRD) analysis (Empyrean, Malvern Panalytical, Almelo, Netherlands) was performed on unreacted particles and particles collected during the immersion experiments. Prior to the analysis, the particles were ground into a fine powder using a mortar and pestle. The analysis utilized nickel-filtered copper K-α radiation (40 kV, 40 mA) and covered a 2θ range of 5.00°–99.98° with a step size of 0.013° and a scan step time of 18.87 s. HighScore Plus software (v4.9) was employed for data analysis. The recorded diffractograms were smoothed using the adaptive denoising function (decomposition level: 4).

2.5.3 | Fourier-Transform Infrared Spectroscopy

As prepared for XRD analysis, powder glass samples were analyzed via Fourier-transform infrared (FTIR) spectroscopy. FTIR spectra were recorded in absorbance mode using a spectrometer (IFS 66S, Bruker optics, Ettlingen, Germany) equipped with a deuterated triglycine sulfate (DTGS) detector and single-bounce attenuated total reflectance (ATR) accessory (VideoMVP, Harrick Scientific Products), employing a diamond crystal with a horizontal sampling area of 0.5 mm^2. Spectra were acquired over the wavenumber range of 300–4000 cm^{-1} with a resolution of 4 cm^{-1}. Each spectrum was obtained from 32 scans. The spectra were smoothened and ATR-corrected using the instrument software (Opus 6.5, Bruker Optics). Intensities were normalized to the highest absorbance values for visual representation.

TABLE 2 | Nominal oxide composition of ZnBG vs. the SEM–EDX-determined oxide composition of the prepared ZnBG particles. The uncertainty of the SEM–EDX measurements is given as ±SD.

	Oxide composition (mol%)				
ZnBG	**Na_2O**	**CaO**	**P_2O_5**	**SiO_2**	**ZnO**
nominal	24.3	24.9	2.6	44.1	4.0
determined	27.1 ± 2.1	24.6 ± 4.7	2.2 ± 0.2	41.9 ± 2.1	4.2 ± 1.0

2.6 | Osteoblast Cell Cultures and Assays

2.6.1 | Cell Culture

MC3T3-E1 pre-osteoblasts (subclone 4; ATCC, CRL-2593) were cultured in T75 flasks in phenol red-free αMEM (Gibco, UK) supplemented with 10% FBS (Gibco, UK) and 1% Penicillin–Streptomycin (Gibco, USA). The cells were grown at 37°C, 5% CO_2, and the media were changed every 2–3 days. Cells between passages 12 and 15 were used in the experiments, and cultures were 80–100% confluent before cells were detached and seeded for viability, fluorescence imaging, and alkaline phosphatase (ALP) activity assays.

2.6.2 | Cell Viability Assay

Before cell seeding, the Ti disks, that is, SA-Ti, APA-Ti, and APA-Ti after 96 h of SBF immersion (CaP-Ti), were washed using 70% ethanol twice (5 min each), followed by a PBS wash (Gibco, UK), then transferred into a 48-well plate and incubated (37°C, 5% CO_2) in cell culture media for 20 min. Cells were detached using 1X trypsin with 0.02% EDTA (Gibco, UK), seeded in triplicates at a density of 13,000 cells per disk, and allowed to grow for up to 7 days. On days 1, 3, and 7, the Alamar Blue (Bio-Rad, USA) assay was performed. Briefly, media were pipetted out, and cells were incubated in 10% Alamar Blue solution (in cell culture media) at 37°C, 5% CO_2 for 4 h; then, 100 μL of each sample was transferred to a 96-well plate in replicates. Fluorescence excitation/emission at 560/590 nm was read using an Ensight Multimode microplate reader (PerkinElmer, USA). Afterward, the Alamar Blue solution was discarded, and cells were washed with PBS. Then, the cells were cultured in fresh cell culture media until the following time point. Cell viability assays were carried out three times with three technical replicates.

2.6.3 | Cell Staining and Fluorescence Imaging

At days 3 and 7, a disk from each group was washed in PBS, and the cells were fixed using 4% paraformaldehyde (Santa Cruz Biotechnology, The Netherlands) for 30 min, then again washed in PBS before being incubated in phalloidin (Actin) (Abcam, UK) (diluted 1:1000 in 1% BSA) for 20 min protected from light. Subsequently, the disks were washed in PBS and incubated for nuclear staining in a 1:100 Hoechst 33258 (Sigma-Aldrich, USA) solution for 10 min, protected from light. Eventually, the disks received a final PBS wash, and fresh PBS was added to each sample. The threaded sides of the disks were viewed using the Evos 5000 Microscope (Invitrogen, USA). The excitation/emission wavelengths used were 470/525 and 357/447 for Actin and Hoechst, respectively.

2.6.4 | Alkaline Phosphatase (ALP) Assay

MC3T3-E1 cells were seeded in triplicates at a density of 20,000 cells per disk and allowed to attach for 24 h, after which the basal media was changed into osteogenic media containing 10 mM beta glycerophosphate, 50 μg/mL ascorbic acid (Sigma-Aldrich, USA), and 0.1 μM dexamethasone (Fisher Scientific, UK). After 7 days, during which the osteogenic media was changed twice, cells were washed with PBS, and 200 μL lysis buffer (50 mM Tris–HCl, 0.1% Triton X-100, 0.9% NaCl) was added to each disk. Cells were then scraped from each disk, and the lysate was transferred to Eppendorf tubes and vortexed for 10 s. The lysates were stored at −80°C until further analysis. Before running the assay, the samples were thawed at room temperature and centrifuged for 15 min (13,000 rpm) at 4°C. P-nitrophenylphosphate (pNPP) (Sigma-Aldrich, USA) was used as an ALP substrate to detect ALP activity. Briefly, 15 μL of pNPP was diluted in 85 μL of assay buffer (0.1 M Tris, 1 mM $MgCl_2$) and added to a fresh 96-well plate (100 μL/well), followed by adding 10 μL of each lysate/well as two assay replicates. The plate was protected from light and incubated at room temperature for 1 h. 1 N NaOH was added to stop the reaction, and then 405 nm absorbance was read using the microplate reader. In order to normalize the ALP levels, DNA quantification was carried out using a Quant-iT dsDNA Assay Kit (ThermoFisher Scientific, USA) according to the manufacturer's instructions, and a standard curve was generated (0–10 ng/μl DNA) to calculate the DNA content for each sample. The ALP assay was conducted three times with three technical replicates, that is, disks.

2.7 | Statistical Analyses

The differences in the proliferation rate among the experimental groups were assessed using a one-way analysis of variance (ANOVA), and the statistical significance was defined as $p < 0.05$. Statistical analyses were conducted using the Statistical Package for the Social Sciences [(SPSS), software version 29.0 (SPSS Inc., Chicago, IL, USA)]. The results are presented as means and standard deviations (SD).

3 | Results

3.1 | Confirmation of the Glass Composition and Particle Size

The as-prepared ZnBG particles were analyzed using SEM–EDX to verify their composition. Elemental analysis was performed on individual particles in 36 different areas. Table 2 compares the nominal oxide composition of ZnBG with the

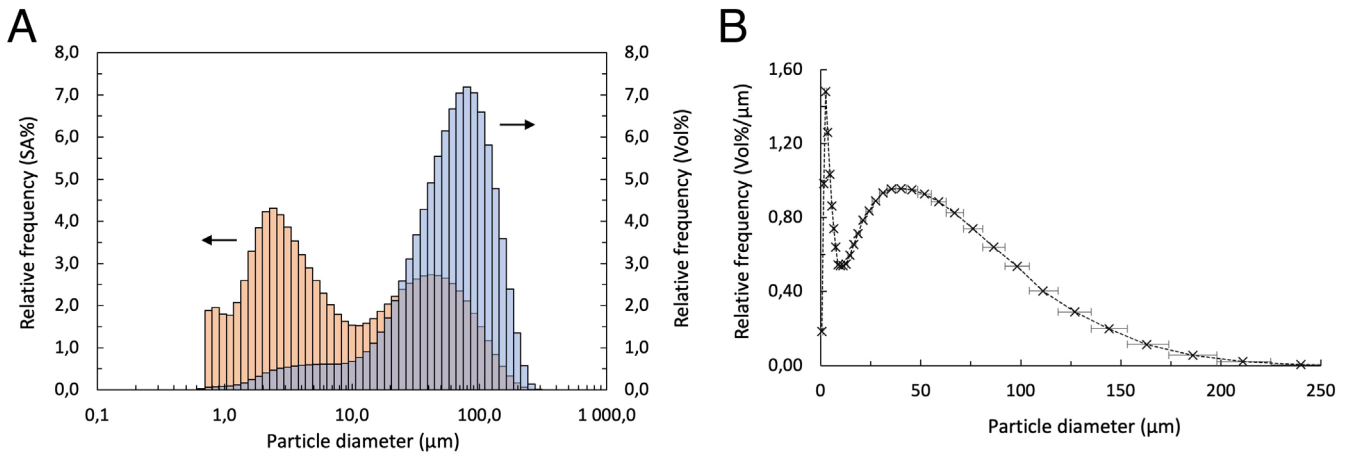

FIGURE 1 | Volume-based particle size distribution (PSD) of the Zn4 particle sample, measured by laser diffraction analysis (LDA). (A) Histogram representation on a logarithmic scale, shown alongside the corresponding surface-area-based PSD. (B) Continuous volume-based PSD curve on a linear scale. Distributions were calculated from 15 repeated measurements ($n = 15$), which showed minimal variation. Standard deviations in relative volume percentage (Vol%) were negligible and are not included in the graphs. Error bars on the x-axis represent the width of the particle size classes.

oxide composition determined for the produced particles. The measured values for CaO, SiO_2, and ZnO were close to the nominal values, particularly when considering measurement uncertainty. However, the measured mole percentage of Na_2O was slightly higher than expected, while that of P_2O_5 was relatively lower. A histogram of the measured volume-based PSD of the ZnBG particle sample, along with the calculated histogram of the surface area-based PSD, is presented in Figure 1A. The x-axis is logarithmically scaled to match the logarithmic spacing of the particle size classes. Figure 1B shows the volume-based PSD as a continuous curve obtained by normalizing the volume share of size classes to equal size class width.

3.2 | Bioactive Glass Immersion Results

3.2.1 | Ion Concentration Profiles

The 96-h concentration profiles of Na, Ca, P, Si, and Zn after immersion of the ZnBG particles and the abraded disks in SBF were measured using ICP-OES. The concentrations of the elements in the initial SBF solution correspond to the respective ion concentration at time 0 h in Figure 2A–E. After 96 h of immersion, the Na concentration had increased by about 6%. The Ca concentration more than doubled within the first 8 h, remaining relatively stable. In contrast, the P concentration steadily decreased, ultimately dropping to less than one-third of the initial level in SBF. The Si concentration increased sharply within the first 8 h, then increased gradually, approaching about 80 mg/L at 96 h. Notably, the Zn concentration remained low throughout the experiment, averaging around 4 mg/mL.

3.2.2 | Surface Composition of Particles During Immersion

The changes in the composition of the ZnBG particle surfaces during the 96-h immersion in SBF are shown in Figures 3A,B. The Si atomic percentage increased during the 96-h immersion, with the most significant increase occurring within the first 8 h. In contrast, the Na atomic percentage dropped sharply during the first 8 h and continued to decrease afterward. The Ca atomic percentage remained relatively constant throughout the experiment. Meanwhile, the P atomic percentage more than doubled during the 96-h period.

3.2.3 | Surface Composition of the APA-Ti Disks During Immersion

The changes in the surface composition of APA-Ti disks during the 96-h immersion in SBF are illustrated in Figure 3C. In the first 8 h, the Ti atomic percentage increased sharply, indicating that the Ti disk surface became partly exposed. A noticeable drop followed this initial rise of the exposed surface, followed by a moderate increase. Simultaneously, the share of Si on the surface was initially relatively low but then increased and reached its highest value at 24 h and decreased slightly thereafter. The Na atomic percentage share drastically reduced in the first 8 h, suggesting almost complete dissolution or detachment of the glass particles attached during APA. Subsequently, the Na atomic percentage increased slightly and remained between 1 and 2 at%. Similarly, the Ca atomic percentage decreased early, though less dramatically than that of Na, before recovering and fluctuating between 2 and 3 at%. In contrast, the P atomic percentage steadily increased at first, reaching 4 to 7 times its initial value, suggesting significant deposition of a phosphorus-containing phase. Meanwhile, the share of Zn at the surface remained at a relatively low level, less than 1 at% throughout the dissolution. Considering that the Ti content was around 80%, the presence of Zn implies that it was successfully incorporated into the surface of the APA-Ti. Figure 3D highlights the changes in the atomic percentages of Ca and P on the surface of the ZnBG abraded disks, along with the changes in the Ca/P atomic ratio.

Figure 4A illustrates the thread configuration of the Ti disks, while Figure 4B shows SEM images of their surface morphology.

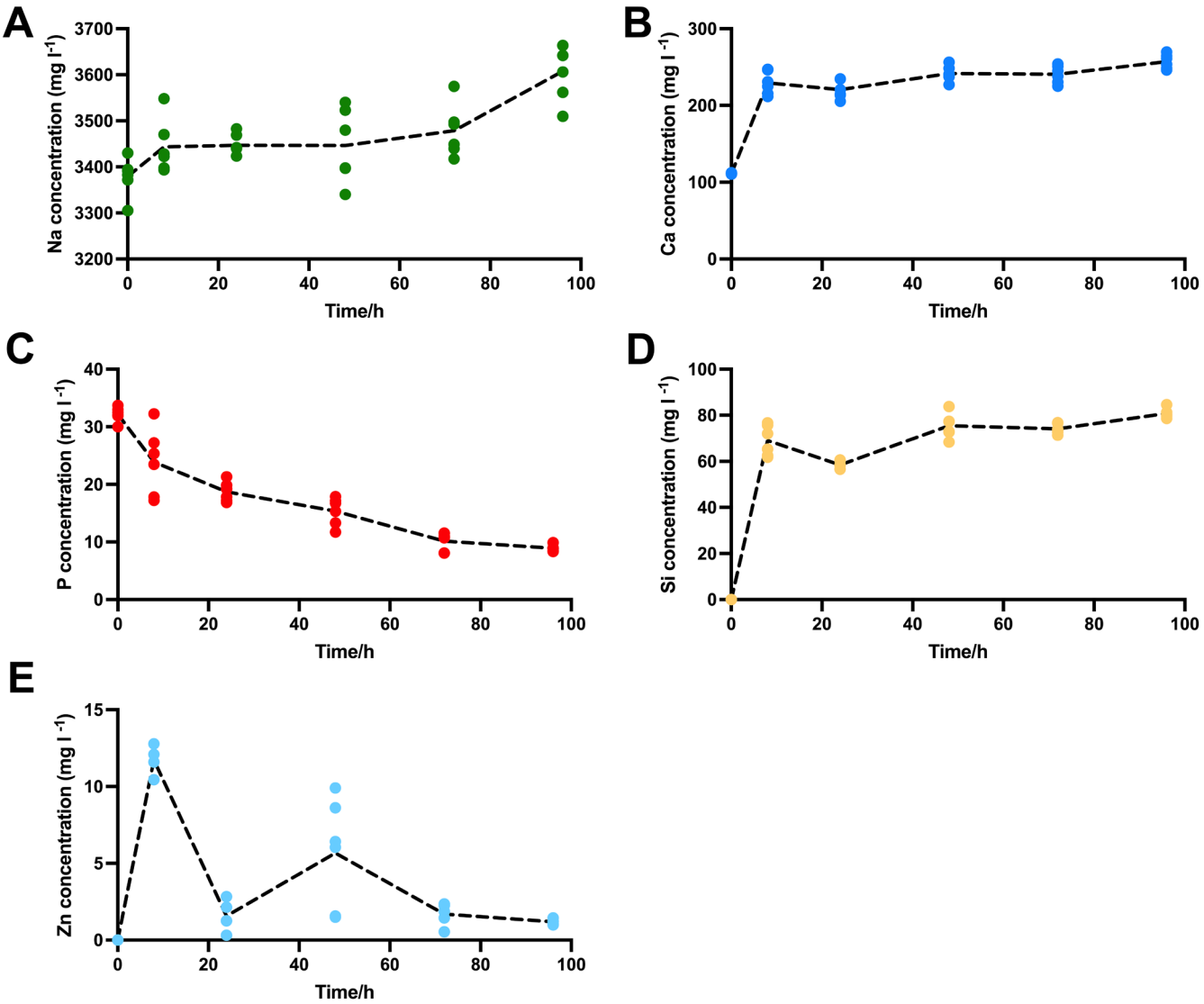

FIGURE 2 | Ion concentration profiles over 96 h for (A) Na, (B) Ca, (C) P, (D) Si, and (E) Zn during immersion of ZnBG particles and ZnBG-abraded titanium disks in simulated body fluid (SBF) at 37°C. Ion concentrations were determined from six independent measurements ($n = 6$). Error bars represent standard deviations.

The SEM analysis revealed that the APA of SA-Ti disks produced a uniform surface topography, which was attributed to BG particles becoming embedded within the surface irregularities of SA-Ti. This characteristic surface pattern remained evident even after APA-Ti disks were immersed in SBF for 96 h, which led to the formation of a Ca–P layer, as observed on the CaP-Ti disks.

3.2.4 | XRD Powder Diffractograms

The XRD powder diffractograms of the ZnBG particles before immersion and after 8, 48, and 96 h of immersion in SBF are displayed in Figure 5A. All diffractograms exhibit a prominent amorphous halo in the 25°–40° 2θ range with a maximum at about 32° 2θ, which is associated with the parent ZnBG phase. As the dissolution progressed, an amorphous shoulder emerged on the left side of this halo, appearing between 18° and 25° 2θ. This shoulder is likely due to the formation of a silica-rich surface alteration layer. No crystalline peaks indicative of hydroxyapatite were observed, even for the longest reaction time.

3.2.5 | FTIR Absorption Spectra

The FTIR absorption spectra of the ZnBG particles before immersion and after 8, 48, and 96 h of immersion in SBF are shown in Figure 5B. The spectrum of the unreacted glass displays several overlapping bands in the 800–1100 cm^{-1} range and a narrower band around 500 cm^{-1}. These bands correspond to the main vibrational modes typical of soda-lime phosphosilicate glasses: asymmetric stretching of Si-O-Si bonds (~990 cm^{-1}), stretching vibrations of Si–O bonds associated with nonbridging oxygen (~922 cm^{-1} and ~854 cm^{-1}) and symmetric bending vibrations of Si–O–Si bonds (~500 cm^{-1}) [21, 22]. As the glass reacted in SBF, the intensity of the Si-O bands associated with nonbridging oxygen gradually decreased. In contrast, the asymmetric stretching band of

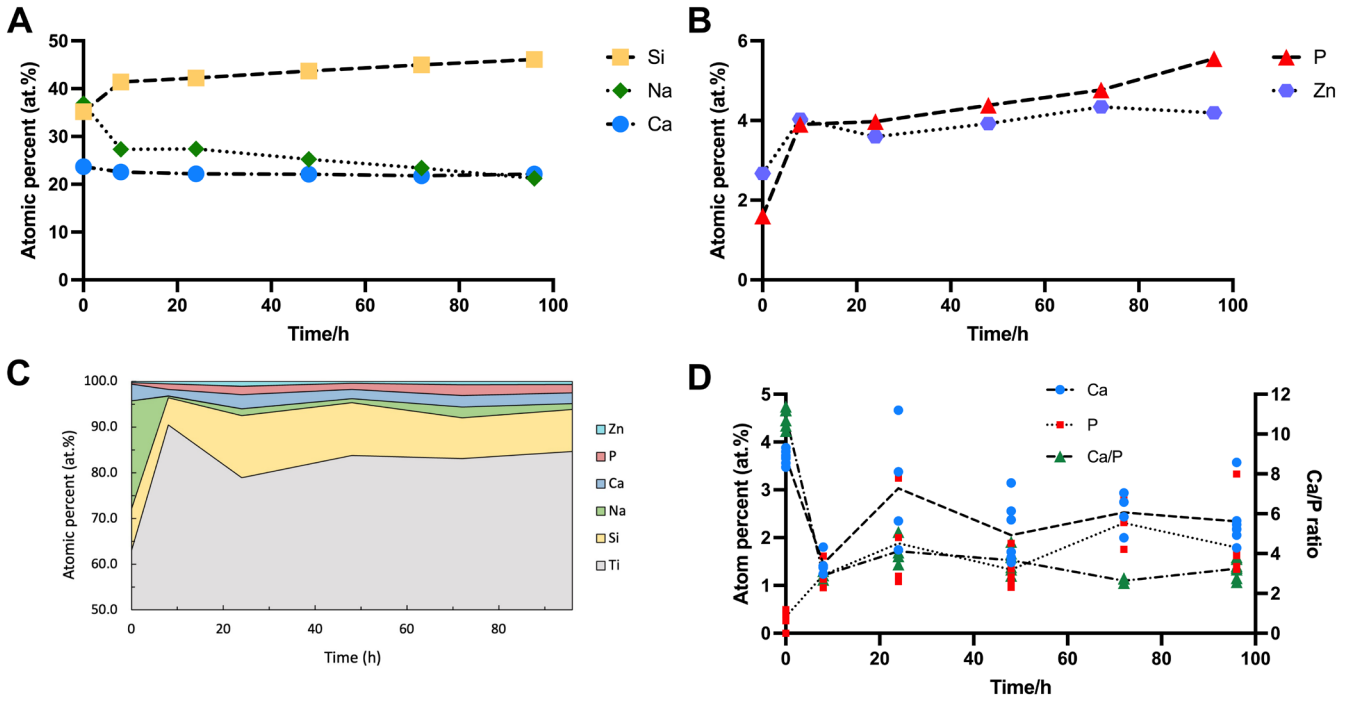

FIGURE 3 | Evolution of surface composition during 96-h immersion in simulated body fluid (SBF), as determined by SEM–EDX. (A, B) Elemental composition of ZnBG particles over time, showing trends for (A) the more abundant elements (Na, Ca, Si) and (B) the less abundant elements (P, Zn). Values represent mean atomic compositions obtained from a single surface area containing a high number of particles; error bars denote ±1 standard deviation, based on statistical variation in X-ray counts. (C) Surface composition of ZnBG-abraded Ti disks (APA-Ti) during immersion, based on SEM–EDX analysis. (D) Changes in atomic percentages of Ca and P on APA-Ti surfaces and the resulting Ca/P ratio over time. Values represent mean compositions determined from five regions ($n = 5$); error bars indicate standard deviations.

Si-O-Si bonds became more distinct and shifted slightly to a higher wavenumber.

3.3 | Osteoblast Cell Viability and Adhesion

3.3.1 | Cell Viability

Pre-osteoblastic MC3T3-E1 cells demonstrated the ability to proliferate on all tested disks, following a similar pattern across the different surface types. Over time, the number of cells increased consistently as the culture time extended. By day 7, a significantly ($p = 0.004$) higher level of cell proliferation was observed on the APA-Ti disks without SBF immersion compared to the SA-Ti. However, there was no statistically significant difference ($p = 0.083$) between APA-Ti and CaP-Ti disks (Figure 6).

3.3.2 | Cell Adhesion

Fluorescence microscope images of cells stained for nuclei and actin cytoskeleton obtained at day 3 indicated that cells on SA-Ti and APA-Ti disks were exclusively spreading in the valleys of the threads (Figure 7). In contrast, cells on the CaP-Ti disks were observed in the valleys and peaks of the threads, with their numbers increasing by day 7. By day 7, cells on the APA-Ti disks were also observed on the peaks of the threads, indicating a shift in their proliferation pattern. However, cells on the SA-Ti disks remained confined to the valleys.

3.3.3 | Alkaline Phosphatase (ALP) Assay

DNA quantification results indicated no statistically significant differences among the tested disks ($p = 0.221$). Nevertheless, there was a trend toward higher DNA content on the APA-Ti surfaces compared to both SA-Ti and CaP-Ti. In comparison, ALP activity, a marker of early osteogenic differentiation, appeared slightly lower on APA-Ti than on SA-Ti and CaP-Ti, although this difference was not statistically significant either ($p = 0.436$) and indicates comparable levels of early osteogenic differentiation capacity across the surfaces (Figure 8).

4 | Discussion

This study demonstrates that the APA of SA-threaded Ti disks using ZnBG effectively supports the proliferation and viability of MC3T3-E1 pre-osteoblasts. However, when these disks were mineralized in SBF for 96 h (CaP-Ti), cell viability levels became comparable to those observed on the nonabraded SA-Ti disks. Yet, there was no statistically significant difference between the APA-Ti and CaP-Ti. These findings indicate that the presence of ZnBG provides a bioactive surface to the abraded disks that promotes cellular proliferation. Osteoblast viability on APA-Ti surfaces was evaluated and compared to that on the same surfaces after 96 h of immersion. This comparison aimed to assess the effect of Ca–P layer deposition on Ti disks on osteoblast cellular activity. Cellular responses were not evaluated

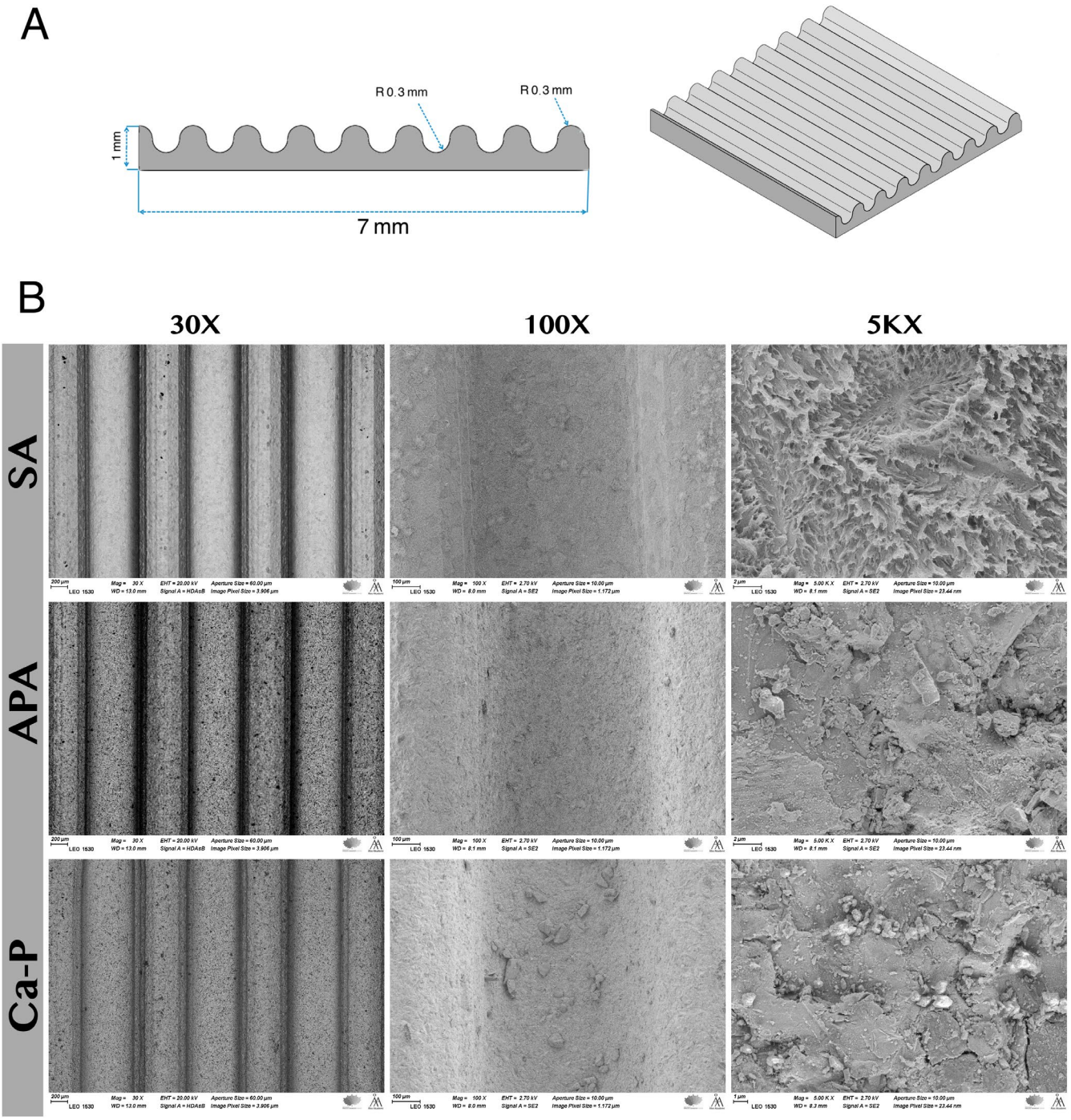

FIGURE 4 | (A) Schematic drawing of the titanium disk threads characteristics. The pitch is 1.0 mm, and depth is 0.3 mm. (B) SEM images of the sandblasted and acid-etched disks (SA-Ti), disks after ZnBG air particle abrasion (APA-Ti), and disks after immersion in SBF for 96 h (CaP-Ti) at 30x, 100x, and 5000x magnifications.

at earlier immersion times, as the ZnBG on the Ti disks may have fully dissolved by then, potentially resulting in biological behavior similar to that of uncoated surfaces (SA-Ti).

The shape and size of BG particles significantly influence the ion dissolution process. Smaller BG particles, with higher specific surface area, dissolve more rapidly, leading to a higher initial ion release. BG microspheres (BGMs) with controlled size and surface area provide better control over ion release kinetics and degradation rates [10, 17, 23]. The continuous curve in Figure 2 shows that the particle sample used for air particle abrasion and in the in vitro dissolution experiments exhibited a bimodal PSD with distinct peaks at approximately 3 μm and 40 μm. This indicates that the sample consisted of two main particle populations: one below 10 μm and another ranging from 10 to 225 μm. The population below 10 μm accounted for approximately 8% of the particle sample's total volume. The presence of fine powder, despite repeated ultrasonic cleaning in acetone, might have been due to the static adhesion of powder to particle surfaces and the agglomeration of powder. Residual amounts of fine powder may have contributed to the sharp initial increase in Ca and Si concentrations during immersion. As shown in Figure 2, the larger

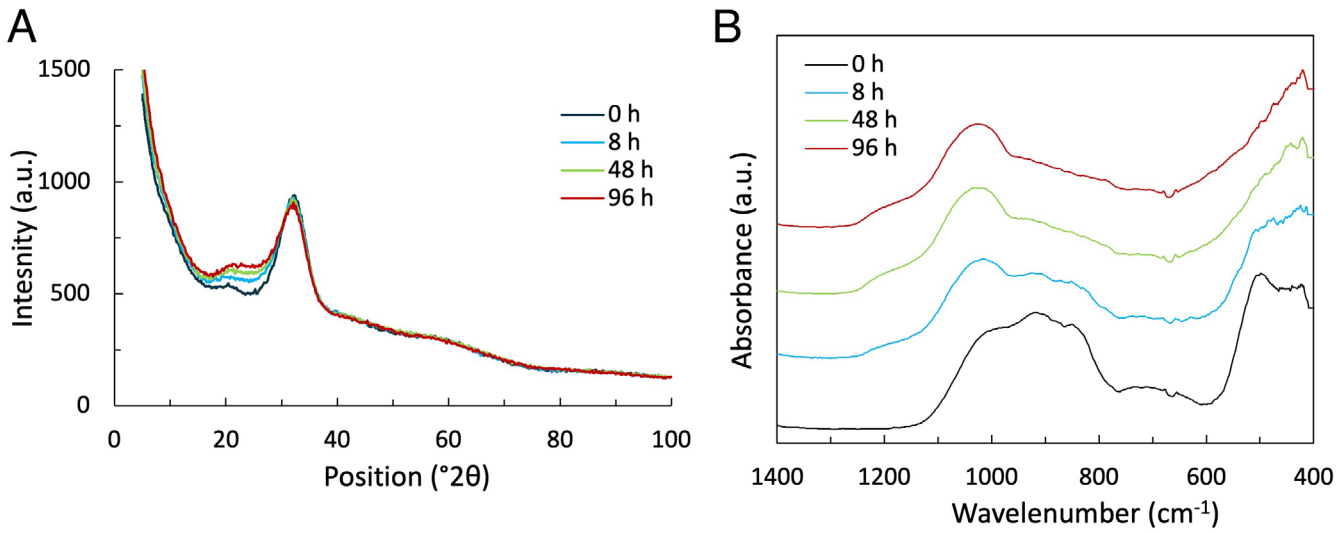

FIGURE 5 | XRD powder diffractograms (A) and FTIR absorption spectra (B) of Zn4 BG particles after different times of immersion in SBF.

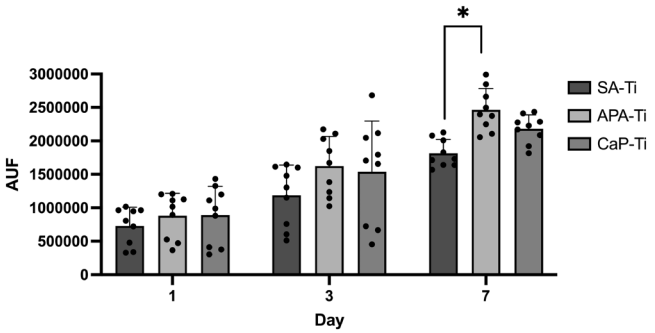

FIGURE 6 | Cell viability assay results of MC3T3-E1 cells cultured on sandblasted and acid-etched (SA-Ti) disks, as well as after ZnBG air particle abrasion of these disks (APA-Ti) and on APA-Ti after SBF immersion for 96-h (CaP-Ti). Data are presented as arbitrary fluorescence units (AFU, 560/590 nm) on days 1, 3, and 7 of cell culture ($n = 9$). The data represent the mean (SD) pooled from three independent cell cultures. P-value (*p = 0.004) indicates the significant difference between groups at the same time point.

particle population covered a broad size range and was notably right-skewed, with a long tail extending toward larger particle sizes. The presence of larger particles suggests that elongated particles passed through the 125 μm sieve openings. Previously, using the setup described herein, the 20–125 μm particle size range has been identified as an optimal range for air particle abrasion based on the requirement for a steady flow through the nozzle. Despite the diversity of particle size distribution, they did not adversely affect the flow of BG from the abrasion device.

Previous studies have shown that Si^{4+} released from BG exhibits stimulatory effects on osteoblasts, including at the gene expression level [24, 25]. Additionally, the gradual release of soluble Si^{4+} over time can improve cytocompatibility and enhance the formation of a porous silica-rich layer on the glass surface, which plays an active role in facilitating the precipitation of Ca–P [25]. In our study, the Si^{4+} concentration and atomic percentage increased sharply in the SBF during the first 8 h of immersion, reaching about 70 mg/L. Furthermore, SEM–EDX analysis showed an increase in the atomic percentage of Si on the surface of the loose ZnBG particles, while FTIR spectral changes suggest polymerization of the remaining silica network following the leaching of network modifiers. Together, these findings indicate the formation of silica-rich surface alteration layers. Notably, in the FTIR spectra, even after 96 h, no P-O bending vibrations around 560 and 604 cm^{-1} were detected, which would have indicated the formation of HA. This may be primarily due to the high SA/V ratio. Ca–P formation on BG is well known to depend on particle dose, with lower SA/V ratios leading to slower but eventually more extensive Ca–P deposition on the glass surface [21, 26]. In contrast, the PO_4^{3-} atomic percentage more than doubled during the 96-h period, suggesting the formation of a mixed layer of silica and Ca–P.

Ca^{2+} is also a vital component and dissolution product of BG, playing a key role in osteoblast activity [27]. This study observed a rapid increase in the Ca^{2+} concentration in SBF due to BG dissolution from 0 to 8 h, and then its concentration remained nearly constant until the end of the dissolution time. The sustained Ca^{2+} availability may account for the enhanced cell proliferation rate observed on freshly ZnBG abraded disks. These results suggest that the bioactivity of the ZnBG relies heavily on its ability to release these ions, which are known to play critical roles in enhancing cellular functions such as proliferation and differentiation, while the stimulatory effects of BG on osteoblasts may be diminished due to the Ca–P layer formation, which reduces ion dissolution. Nevertheless, secondary Ca–P phases at the particle surface can also dissolve and release Ca^{2+} and PO_4^{3-} into the surrounding solution, potentially promoting osteoblast proliferation [28]. Ca–P materials used in biomedical applications exhibit varying Ca/P molar ratios, ranging from 0.5 in brushite to 1.67 in HA. Ceramics with a Ca/P molar ratio between 1.59 and 1.67 have been shown to significantly enhance osteoblast proliferation [29, 30]. In this study, the Ca/P ratio on the Ti disks, as determined by SEM–EDX, was between 1.1 and 1.6 for immersion times between 24 and 96 h. The Ca/P ratio generally remaining below 1.6 may be attributed to the short immersion duration.

The surface composition of the disks immersed in SBF consistently changed throughout the 96-h immersion time, with the atomic percentages of glass elements decreased sharply at the

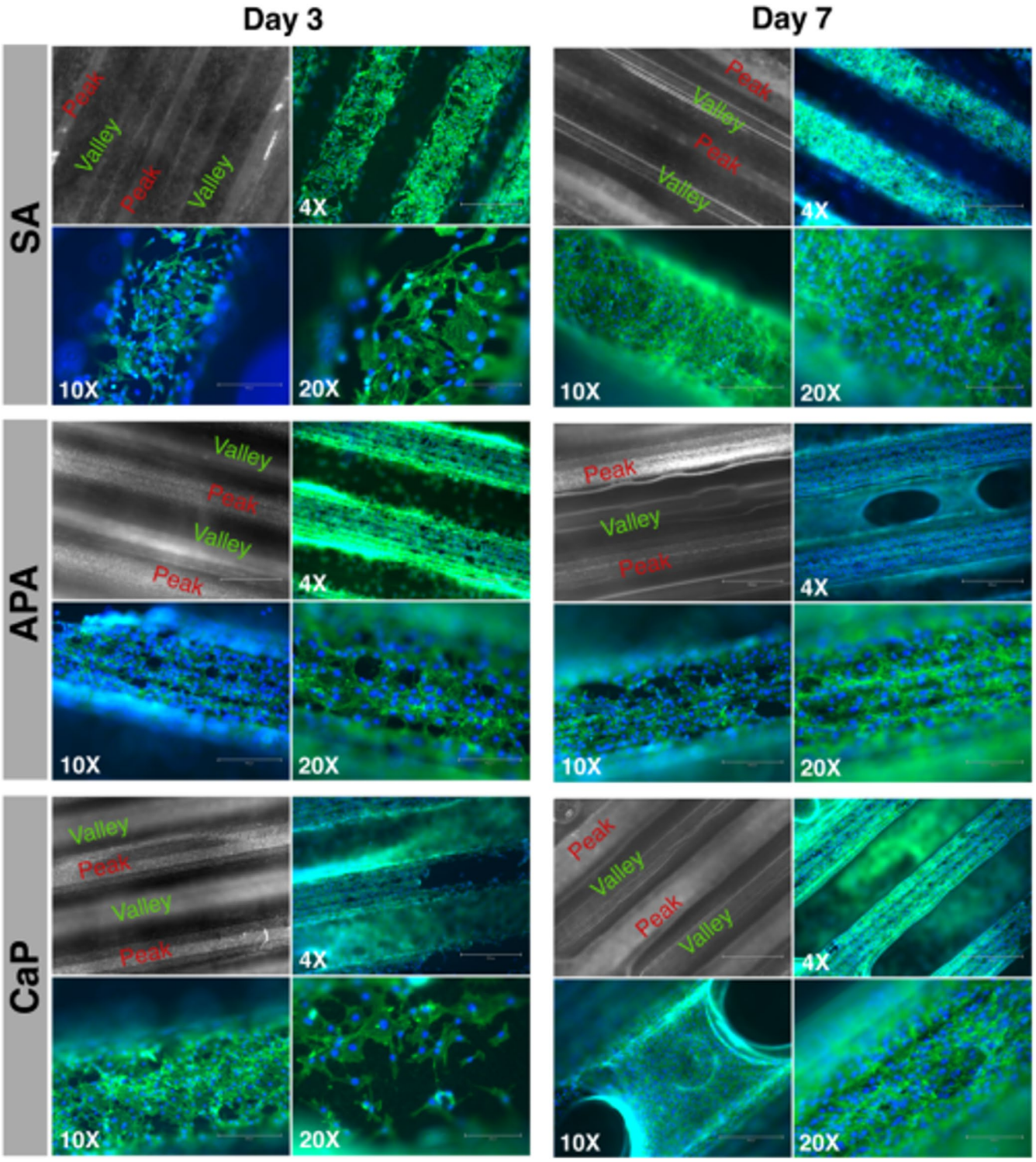

FIGURE 7 | Fluorescence microscope images of MC3T3-E1 cells cultured for 3 and 7 days on sandblasted and acid-etched (SA-Ti) disks as well as on SA-Ti disks after ZnBG air particle abrasion (APA-Ti) and on APA-Ti after SBF immersion for 96 h (CaP-Ti). Cytoskeletal Actin is stained green, while nuclei are blue. Magnifications (4X; scale bar 800 μm, 10X; scale bar 450 μm and 20X; scale bar 200 μm) are implicated in images.

first 8 h, indicating that the ZnBG, which covered the Ti disks, partly dissolved in SBF. As time extended, the percentages of Si, Ca, and P elements moderately increased. The changes in the surface composition suggest complex interactions between the Ti surface, the initial glass fragments attached to it, and the surrounding solution, which can be interpreted in terms of three distinct phases. In the initial phase (0–8 h), there is a significant reduction in the atomic percentages of the ZnBG elements, accompanied by a sharp increase in the Ti atomic percentage. This likely resulted from the rapid initial dissolution of ZnBG fragments attached to the Ti surface after APA. In the second phase (8–24 h), the Ti atomic percentage decreased as the surface became more covered again by elements precipitated from the solution, such as Ca, P, and Si. In the late phase (24–96 h),

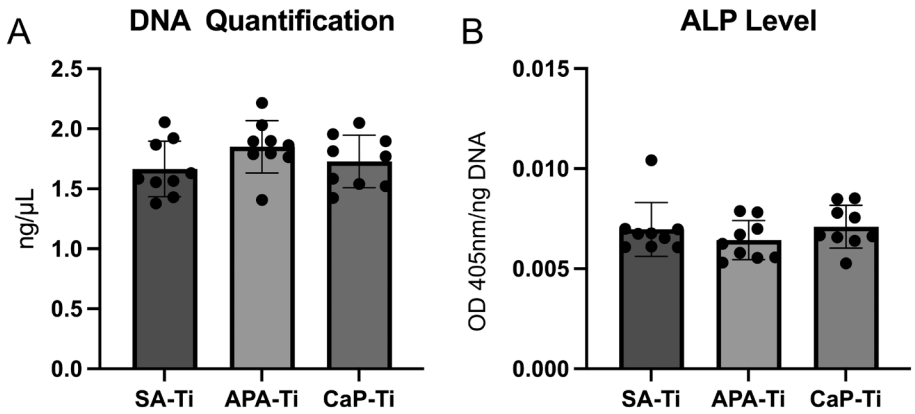

FIGURE 8 | DNA quantification (A) and alkaline phosphatase (ALP) levels (B) of MC3T3-E1 cells cultured for 7 days on sandblasted and acid-etched (SA-Ti) disks, as well as after ZnBG air particle abrasion of these disks (APA-Ti) and on APA-Ti after SBF immersion for 96-h (CaP-Ti). The data represent the mean (SD) pooled from three independent cell cultures ($n = 9$).

the surface composition appears to have stabilized, probably because an equilibrium was reached between the dissolution and deposition of the secondary phases on the plates.

In this study, we utilized threaded SA-Ti disks to replicate the surface characteristics of commercially available dental implants, ensuring that the experimental conditions mimic real clinical scenarios at least to a certain extent. It has been demonstrated that osteoblast cells first settle on the valleys of the implant surface threads due to their weight. Then, the cells attach and spread across the surface while proliferating [31]. Previous studies have also shown that osteoblasts favor microgrooves for growth, as these structures can guide their alignment and cellular extensions, influence the formation and positioning of focal adhesions, and regulate extracellular matrix production [32, 33]. In this study, the fluorescence imaging demonstrated that MC3T3-E1 pre-osteoblasts could grow in the thread's valleys of all disks. In addition, the cells were also able to reach the thread peaks on the third day for the CaP-Ti disks and on the seventh day for the APA-Ti disks. This observation suggests that the Ca–P surface layer developed during SBF immersion favored earlier cell adhesion and spreading compared to other groups. A previous study by Kobayashi et al. [34] investigated the behavior of MC3T3-E1 pre-osteoblasts on Ti surfaces coated with various ratios of Ca–P compositions and found that cell proliferation decreases as the Ca/P ratio increases. In the current study, the Ca/P molar ratio after 96 h of SBF immersion was 1.3. Since the Ca/P molar ratio of HA is 1.67 [35, 36], a ratio of 1.3 indicates the presence of a Ca-deficient layer on the surface, which could contribute to our observations on cell proliferation.

Biologically, Zn^{2+} is a crucial element that has been shown to stimulate the proliferation and differentiation of osteoblastic MC3T3-E1 cells [37]. The cellular mechanisms by which zinc promotes osteoblasts are not fully understood. However, supplementation of cell culture medium with zinc has been found to enhance mineralization and the expression levels of osteocalcin mRNA in MC3T3-E1 cells [37, 38]. Previous studies have shown that Zn^{2+} benefits the proliferation of MC3T3-E1 cells in the 1% to 20% zinc concentration range. Studies by Zhong and Ma [39] and Wang et al. [40] reported that the effect of Zn^{2+} was dose-dependent as cell proliferation increased in samples with a higher Zn^{2+} concentration (5% and 0.56 M, respectively). In contrast, data from another study suggested that the HA layer with 15% of Zn^{2+} negatively affected pre-osteoblast proliferation [41]. Interestingly, in the present study, the atomic percentage of Zn^{2+} was increased after immersion from 2.7% to 3.9%, indicating that Zn^{2+} may incorporate into the mixed layer. Nevertheless, in the current study, cell proliferation was significantly higher on the APA-Ti disks, whereas cell adhesion and spreading were more pronounced on the CaP-Ti disks.

The DNA quantification data supported the cell viability results for MC3T3-E1 pre-osteoblasts. On day 7, APA-Ti disks showed slightly higher DNA content compared to SA-Ti and CaP-Ti disks, indicating higher cell proliferation. Furthermore, assessment of ALP activity showed that both APA-Ti and CaP-Ti disks supported osteoblast differentiation with no significant differences compared to the SA-Ti control. ALP is an early osteoblast differentiation marker, facilitating the downstream osteogenic differentiation and matrix mineralization [39]. Ortega et al. [42] have previously demonstrated that sandblasting and acid-etching of Ti surfaces significantly enhance ALP expression compared to either method alone.

Additionally, Ca–P coatings have been shown to significantly increase ALP levels at Ca/P ratios ranging from 0.5 to 2.5 [43], and incorporating zinc into HA silk-fibroin scaffolds has been reported to enhance ALP activity dose-dependently [39]. Although a slight reduction in ALP activity was noticed on APA-Ti disks, this corresponded with the increased cell proliferation both in basal and osteogenic media. Indeed, the proliferation rate is known to decline during osteogenic differentiation, which explains the slight decrease in ALP activity within the APA-Ti group and may reflect a shift toward higher proliferation rather than reduced differentiation [44]. Additionally, changes in surface topography, such as those introduced by ZnBG and Ca–P coatings, can influence osteoblast proliferation and differentiation [39], with rougher surfaces known to enhance ALP expression [42]. Given these observations, it is likely that under the current experimental conditions, sandblasting, acid etching, and CaP deposition could promote MC3T3-E1 differentiation, while APA-Ti surfaces tend to favor cell proliferation.

It is important to highlight that various implant surface characteristics, including surface roughness, wettability, and surface

free energy (SFE), play an essential role in osteoblast proliferation and differentiation [42, 45]. The surface roughness induced by the SA surface modification process is known to influence both wettability and SFE, significantly impacting cell attachment and differentiation [46–48]. A high SFE with a dominant polar component corresponding to a lower contact angle (CA) and increased surface wettability enhances interactions with the surrounding biological environment [49]. However, the current study did not address these surface characteristics and their effect on cellular responses. It should also be noted that this study was conducted under in vitro conditions, which provide valuable insights into cellular responses and material interactions but do not fully reproduce the complexity of the physiological environment. Therefore, further in vivo studies are warranted to confirm these findings and to assess their clinical relevance.

5 | Conclusions

Within the limitations of this study, it can be concluded that air particle abrasion of sandblasted and acid-etched titanium surfaces supported osteoblast proliferation, adhesion, spreading, and differentiation. Under the given in vitro conditions, bioactive glass particles on the abraded titanium disks dissolve rapidly within 8 h, leading to the subsequent precipitation of a calcium phosphate layer from the surrounding solution. This layer exhibited biocompatibility by promoting osteoblast adhesion. Despite the formation of a Ca–P layer, no hydroxyapatite was observed.

Author Contributions

Faleh Abushahba: conceptualization, data curation, formal analysis, investigation, methodology, visualization, writing – original draft. **Adrian Stiller:** data curation, formal analysis, investigation, methodology, visualization, writing – original draft. **Sherif A. Mohamad:** data curation, formal analysis, investigation, methodology, visualization, writing – original draft. **Nagat Areid:** methodology, eriting – review and editing. **Leena Hupa:** resources, writing – review and editing. **Terhi J. Heino:** resources, supervision, writing – review and editing. **Pekka K. Vallittu:** resources, supervision, writing – review and editing. **Timo O. Närhi:** conceptualization, methodology, supervision, writing – review and editing. All authors have given approval to the final version of the manuscript.

Acknowledgments

This research is funded by Business Finland Co-innovation—project number IMD1 11/31/2023.

Conflicts of Interest

The authors declare no conflicts of interest.

Data Availability Statement

The data that support the findings of this study are available from the corresponding author upon reasonable request.

References

1. D. Herrera, T. Berglundh, F. Schwarz, et al., “Prevention and Treatment of Peri-Implant Diseases—The <Scp>EFP S3</Scp> Level Clinical Practice Guideline,” *Journal of Clinical Periodontology* 50 (2023): 4–76, https://doi.org/10.1111/jcpe.13823.

2. N. de Campos Kajimoto, Y. Paiva Buischi, M. Mohamadzadeh, and P. Loomer, “The Oral Microbiome of Peri-Implant Health and Disease: A Narrative Review,” *Dentistry Journal* 12 (2024): 299, https://doi.org/10.3390/dj12100299.

3. T. Berglundh, G. Armitage, M. G. Araujo, et al., “Peri-Implant Diseases and Conditions: Consensus Report of Workgroup 4 of the 2017 World Workshop on the Classification of Periodontal and Peri-Implant Diseases and Conditions,” *Journal of Clinical Periodontology* 45 (2018): S286-S291, https://doi.org/10.1111/jcpe.12957.

4. S. Kligman, Z. Ren, C.-H. Chung, et al., “The Impact of Dental Implant Surface Modifications on Osseointegration and Biofilm Formation,” *Journal of Clinical Medicine* 10 (2021): 1641, https://doi.org/10.3390/jcm10081641.

5. Y.-M. Yu, Y.-P. Lu, T. Zhang, Y.-F. Zheng, Y.-S. Liu, and D.-D. Xia, “Biomaterials Science and Surface Engineering Strategies for Dental Peri-Implantitis Management,” *Military Medical Research* 11 (2024): 29, https://doi.org/10.1186/s40779-024-00532-9.

6. F. Abushahba, M. Gürsoy, L. Hupa, and T. O. Närhi, “Effect of Bioactive Glass Air-Abrasion on Fusobacterium Nucleatum and *Porphyromonas Gingivalis* Biofilm Formed on Moderately Rough Titanium Surface,” *European Journal of Oral Sciences* 129 (2021): 12783, https://doi.org/10.1111/eos.12783.

7. F. Abushahba, E. Söderling, L. Aalto-Setälä, L. Hupa, and T. O. Närhi, “Air Abrasion With Bioactive Glass Eradicates *Streptococcus Mutans* Biofilm From a Sandblasted and Acid-Etched Titanium Surface,” *Journal of Oral Implantology* 45 (2019): 444–450, https://doi.org/10.1563/aaid-joi-D-18-00324.

8. F. Abushahba, N. Areid, M. Gürsoy, et al., “Bioactive Glass Air-Abrasion Promotes Healing Around Contaminated Implant Surfaces Surrounded by Circumferential Bone Defects: An Experimental Study in the Rat,” *Clinical Implant Dentistry and Related Research* 25 (2023): 409–418, https://doi.org/10.1111/cid.13172.

9. F. Abushahba, E. Söderling, L. Aalto-Setälä, J. Sangder, L. Hupa, and T. O. Närhi, “Antibacterial Properties of Bioactive Glass Particle Abraded Titanium Against *Streptococcus Mutans*,” *Biomedical Physics & Engineering Express* 4 (2018): 045002, https://doi.org/10.1088/2057-1976/aabeee.

10. M. Siekkinen, O. Karlström, and L. Hupa, “Effect of Local Ion Concentrations on the In Vitro Reactions of Bioactive Glass 45S5 Particles,” *International Journal of Applied Glass Science* 13 (2022): 695–707, https://doi.org/10.1111/ijag.16579.

11. P. Sepulveda, J. R. Jones, and L. L. Hench, “In Vitro Dissolution of Melt-Derived 45S5 and Sol-Gel Derived 58S Bioactive Glasses,” *Journal of Biomedical Materials Research* 61 (2002): 301–311, https://doi.org/10.1002/jbm.10207.

12. P. Stoor, E. Soderling, and J. I. Salonen, “Antibacterial Effects of a Bioactive Glass Paste on Oral Microorganisms,” *Acta Odontologica Scandinavica* 56 (1998): 161–165.

13. I. Allan, H. Newman, and M. Wilson, “Antibacterial Activity of Particulate Bioglass Against Supra- and Subgingival Bacteria,” *Biomaterials* 22, no. 12 (2001): 1683–1687.

14. I. Allan, H. Newman, and M. Wilson, “Particulate Bioglass Reduces the Viability of Bacterial Biofilms Formed on Its Surface in an In Vitro Model,” *Clinical Oral Implants Research* 13 (2002): 53–58.

15. L. L. Hench, “Bioceramics: From Concept to Clinic,” *Journal of the American Ceramic Society* 74 (1991): 1487–1510, https://doi.org/10.1111/j.1151-2916.1991.tb07132.x.

16. L. L. Hench, “The Story of Bioglass,” *Journal of Materials Science: Materials in Medicine* 17 (2006): 967–978, https://doi.org/10.1007/s10856-006-0432-z.

17. P. Sinitsyna, O. Karlström, C. Sevonius, and L. Hupa, “In Vitro Dissolution and Characterisation of Flame-Sprayed Bioactive Glass

Microspheres S53P4 and 13–93," *Journal of Non-Crystalline Solids* 591 (2022): 121736, https://doi.org/10.1016/j.jnoncrysol.2022.121736.

18. F. Abushahba, J. Tuukkanen, L. Aalto-Setälä, I. Miinalainen, L. Hupa, and T. O. Närhi, "Effect of Bioactive Glass Air-Abrasion on the Wettability and Osteoblast Proliferation on Sandblasted and Acid-Etched Titanium Surfaces," *European Journal of Oral Sciences* 128 (2020): 160–169, https://doi.org/10.1111/eos.12683.

19. F. Abushahba, E. Kylmäoja, N. Areid, et al., "Osteoblast Attachment on Bioactive Glass Air Particle Abrasion-Induced Calcium Phosphate Coating," *Bioengineering* 11 (2024): 74, https://doi.org/10.3390/bioengineering11010074.

20. T. Kokubo and H. Takadama, "How Useful Is SBF in Predicting In Vivo Bone Bioactivity?," *Biomaterials* 27 (2006): 2907–2915, https://doi.org/10.1016/j.biomaterials.2006.01.017.

21. J. R. Jones, P. Sepulveda, and L. L. Hench, "Dose-Dependent Behavior of Bioactive Glass Dissolution," *Journal of Biomedical Materials Research* 58 (2001): 720–726, https://doi.org/10.1002/jbm.10053.

22. D. S. Brauer, R. Brückner, M. Tylkowski, and L. Hupa, "Sodium-Free Mixed Alkali Bioactive Glasses," *Biomedical Glasses* 2 (2016): 2, https://doi.org/10.1515/bglass-2016-0012.

23. M. Borden, L. E. Westerlund, V. Lovric, and W. Walsh, "Controlling the Bone Regeneration Properties of Bioactive Glass: Effect of Particle Shape and Size," *Journal of Biomedical Materials Research. Part B, Applied Biomaterials* 110 (2022): 910–922, https://doi.org/10.1002/jbm.b.34971.

24. P. E. Keeting, M. J. Oursler, K. E. Wiegand, S. K. Bonde, T. C. Spelsberg, and B. L. Riggs, "Zeolite a Increases Proliferation, Differentiation, and Transforming Growth Factor β Production in Normal Adult Human Osteoblast-Like Cells In Vitro," *Journal of Bone and Mineral Research* 7 (1992): 1281–1289, https://doi.org/10.1002/jbmr.5650071107.

25. I. D. Xynos, A. J. Edgar, L. D. K. Buttery, L. L. Hench, and J. M. Polak, "Gene-Expression Profiling of Human Osteoblasts Following Treatment With the Ionic Products of Bioglass 45S5 Dissolution," *Journal of Biomedical Materials Research* 55 (2001): 151–157, https://doi.org/10.1002/1097-4636(200105)55:2<151::AID-JBM1001>3.0.CO;2-D.

26. Ö. H. Andersson, K. Vähätalo, A. Yli-Urpo, R.-P. Happonen, and K. H. Karlsson, "Short-Term Reaction Kinetics of Bioactive Glass in Simulated Body Fluid and in Subcutaneous Tissue," *Bioceramics, Elsevier* 7 (1994): 67–72, https://doi.org/10.1016/B978-0-08-042144-5.50014-5, Elsevier.

27. Y. Hao, N. Yang, M. Sun, S. Yang, and X. Chen, "The Role of Calcium Channels in Osteoporosis and Their Therapeutic Potential," *Frontiers in Endocrinology* 15 (2024): 1450328, https://doi.org/10.3389/fendo.2024.1450328.

28. X. Wang, Y. Yu, L. Ji, Z. Geng, J. Wang, and C. Liu, "Calcium Phosphate-Based Materials Regulate Osteoclast-Mediated Osseointegration," *Bioactive Materials* 6 (2021): 4517–4530, https://doi.org/10.1016/j.bioactmat.2021.05.003.

29. I. Bajpai, D. Y. Kim, K.-J. J, I. Song, and S. Kim, "Response of Human Bone Marrow-Derived MSCs on Triphasic ca-P Substrate With Various HA/TCP Ratio," *Journal of Biomedical Materials Research. Part B, Applied Biomaterials* 105 (2017): 72–80, https://doi.org/10.1002/jbm.b.33538.

30. A. Pandit, A. Indurkar, J. Locs, H. J. Haugen, and D. Loca, "Calcium Phosphates: A Key to Next-Generation In Vitro Bone Modeling," *Advanced Healthcare Materials* 13 (2024): 13, https://doi.org/10.1002/adhm.202401307.

31. H. J. Jeon, A. Jung, H. J. Kim, et al., "Enhanced Osteoblast Adhesion and Proliferation on Vacuum Plasma-Treated Implant Surface," *Applied Sciences* 12 (2022): 9884, https://doi.org/10.3390/app12199884.

32. T. Stich, F. Alagboso, T. Křenek, T. Kovářík, V. Alt, and D. Docheva, "Implant-Bone-Interface: Reviewing the Impact of Titanium Surface Modifications on Osteogenic Processes In Vitro and In Vivo," *Bioengineering & Translational Medicine* 7 (2022): 10239, https://doi.org/10.1002/btm2.10239.

33. K. Matsuzaka, X. Frank Walboomers, M. Yoshinari, T. Inoue, and J. A. Jansen, "The Attachment and Growth Behavior of Osteoblast-Like Cells on Microtextured Surfaces," *Biomaterials* 24 (2003): 2711–2719, https://doi.org/10.1016/S0142-9612(03)00085-1.

34. M. Kobayashi, S. Nihonmatsu, T. Okawara, et al., "Adhesion and Proliferation of Osteoblastic Cells on Hydroxyapatite-Dispersed Ti-Based Composite Plate," *In Vivo (Brooklyn)* 33 (2019): 1067–1679, https://doi.org/10.21873/invivo.11575.

35. S. Raynaud, E. Champion, D. Bernache-Assollant, and P. Thomas, "Calcium Phosphate Apatites With Variable ca/P Atomic Ratio I. Synthesis, Characterisation and Thermal Stability of Powders," *Biomaterials* 23 (2002): 1065–1072, https://doi.org/10.1016/S0142-9612(01)00218-6.

36. H. Guo, J. Wei, Y. Yuan, and C. Liu, "Development of Calcium Silicate/Calcium Phosphate Cement for Bone Regeneration," *Biomedical Materials* 2 (2007): S153–S159, https://doi.org/10.1088/1748-6041/2/3/S13.

37. M. Yamaguchi and M. N. Weitzmann, "Zinc Stimulates Osteoblastogenesis and Suppresses Osteoclastogenesis by Antagonizing NF-κB Activation," *Molecular and Cellular Biochemistry* 355 (2011): 179–186, https://doi.org/10.1007/s11010-011-0852-z.

38. D. L. Bouglé, J.-P. Sabatier, G. Guaydier-Souquières, et al., "Zinc Status and Bone Mineralisation in Adolescent Girls," *Journal of Trace Elements in Medicine and Biology* 18 (2004): 17–21, https://doi.org/10.1016/j.jtemb.2004.03.001.

39. Z. Zhong and J. Ma, "Fabrication, Characterization, and In Vitro Study of Zinc Substituted Hydroxyapatite/Silk Fibroin Composite Coatings on Titanium for Biomedical Applications," *Journal of Biomaterials Applications* 32 (2017): 399–409, https://doi.org/10.1177/0885328217723501.

40. X. Wang, A. Ito, Y. Sogo, X. Li, and A. Oyane, "Zinc-Containing Apatite Layers on External Fixation Rods Promoting Cell Activity," *Acta Biomaterialia* 6 (2010): 962–968, https://doi.org/10.1016/j.actbio.2009.08.038.

41. M. Okada, M. Oshita, M. Kataoka, Y. Azuma, and T. Furuzono, "Shareability of Antibacterial and Osteoblastic-Proliferation Activities of Zinc-Doped Hydroxyapatite Nanoparticles In Vitro," *Journal of Biomedical Materials Research. Part B, Applied Biomaterials* 110 (2022): 799–805, https://doi.org/10.1002/jbm.b.34959.

42. E. Velasco-Ortega, I. Fos-Parra, D. Cabanillas-Balsera, et al., "Osteoblastic Cell Behavior and Gene Expression Related to Bone Metabolism on Different Titanium Surfaces," *International Journal of Molecular Sciences* 24 (2023): 3523, https://doi.org/10.3390/ijms24043523.

43. H. Liu, H. Yazici, C. Ergun, T. J. Webster, and H. Bermek, "An In Vitro Evaluation of the ca/P Ratio for the Cytocompatibility of Nano-To-Micron Particulate Calcium Phosphates for Bone Regeneration," *Acta Biomaterialia* 4 (2008): 1472–1479, https://doi.org/10.1016/j.actbio.2008.02.025.

44. A. W. Robert, B. H. Marcon, B. Dallagiovanna, and P. Shigunov, "Adipogenesis, Osteogenesis, and Chondrogenesis of Human Mesenchymal Stem/Stromal Cells: A Comparative Transcriptome Approach," *Frontiers in Cell and Developmental Biology* 8 (2020): 561, https://doi.org/10.3389/fcell.2020.00561.

45. K. P. Nobles, A. V. Janorkar, and R. S. Williamson, "Surface Modifications to Enhance Osseointegration–Resulting Material Properties and Biological Responses," *Journal of Biomedical Materials Research. Part B, Applied Biomaterials* 109 (2021): 1909–1923, https://doi.org/10.1002/jbm.b.34835.

46. M. Pegueroles, C. Aparicio, M. Bosio, et al., "Spatial Organization of Osteoblast Fibronectin Matrix on Titanium Surfaces: Effects of Roughness, Chemical Heterogeneity and Surface Energy," *Acta Biomaterialia* 6 (2010): 291–301, https://doi.org/10.1016/j.actbio.2009.07.030.

47. J. Lin, H. Dong, Y. Wen, X. Zhuang, and S. Li, "Surface Free Energy of Titanium Disks Enhances Osteoblast Activity by Affecting the Conformation of Adsorbed Fibronectin," *Frontiers in Materials* 9 (2022): 9, https://doi.org/10.3389/fmats.2022.840813.

48. I. Abrahamsson, N. U. Zitzmann, T. Berglundh, E. Linder, A. Wennerberg, and J. Lindhe, "The Mucosal Attachment to Titanium Implants With Different Surface Characteristics: An Experimental Study in Dogs," *Journal of Clinical Periodontology* 29 (2002): 448–455, https://doi.org/10.1034/j.1600-051X.2002.290510.x.

49. D. Bociaga, A. Sobczyk-Guzenda, P. Komorowski, et al., "Surface Characteristics and Biological Evaluation of Si-DLC Coatings Fabricated Using Magnetron Sputtering Method on Ti6Al7Nb Substrate," *Nanomaterials* 9 (2019): 812, https://doi.org/10.3390/nano9060812.